

**Doctoral Thesis**

**Optical Follow-Up of High-Energy Neutrinos**

Simeon Reusch

March 24, 2023

Humboldt-Universität zu Berlin

## **Copyright**

©@ This book is released into the public domain using the CC0 code. To the extent possible under law, I waive all copyright and related or neighbouring rights to this work. To view a copy of the CC0 code, visit: <http://creativecommons.org/publicdomain/zero/1.0>

This thesis was typeset with the help of KOMA-Script and L<sup>A</sup>T<sub>E</sub>X using the kaobook class.

The code used to typeset this thesis and create the figures within can be accessed at [github.com/simeonreusch/thesis](https://github.com/simeonreusch/thesis)

## **Publisher**

First published in August 2023 by Humboldt-Universität zu Berlin

# Contents

<b>Contents</b>	<b>iii</b>
<b>1 The IceCube Detector</b>	<b>1</b>
1.1 Cherenkov radiation . . . . .	1
1.2 Instrumentation . . . . .	2
1.2.1 Photomultiplier tubes . . . . .	2
1.2.2 The Digital Optical Module . . . . .	3
1.2.3 Detector layout . . . . .	4
1.2.4 Deployment . . . . .	4
1.2.5 The IceTop surface array . . . . .	5
1.2.6 Data acquisition . . . . .	5
1.2.7 Time synchronization . . . . .	5
1.3 Angular Reconstruction . . . . .	6
1.3.1 Event types . . . . .	6
1.3.2 Likelihood approach . . . . .	6
1.3.3 Single photoelectron fit . . . . .	8
1.3.4 Multi photoelectron fit . . . . .	8
1.4 The Realtime Alert Program . . . . .	8
1.4.1 Background . . . . .	9
1.4.2 Event selection . . . . .	9
1.4.3 Alert distribution . . . . .	10
<b>2 The Zwicky Transient Facility</b>	<b>11</b>
2.1 Telescope Design . . . . .	12
2.2 Camera . . . . .	13
2.3 Optical System . . . . .	14
2.4 Calibration and Image Processing . . . . .	15
2.5 Surveys and Cadence . . . . .	20
<b>APPENDIX</b>	<b>21</b>
<b>Bibliography</b>	<b>23</b>



# List of Figures

1.1	Cherenkov radiation . . . . .	1
1.2	Cherenkov spectrum . . . . .	2
1.3	PMT schematic . . . . .	2
1.4	IceCube digital optical module . . . . .	3
1.5	IceCube DOM connections . . . . .	3
1.6	IceCube side-on . . . . .	4
1.7	IceCube top-down view . . . . .	4
1.8	IceCube enhanced hot water drill . . . . .	5
1.9	IceTop detector . . . . .	5
1.10	Track event in IceCube . . . . .	6
1.11	Cascade event in IceCube . . . . .	6
1.12	Angular reconstruction in IceCube . . . . .	7
1.13	Background events . . . . .	9
1.14	Muon free path in ice . . . . .	9
1.15	Neutrino absorption in the earth . . . . .	9
1.16	HESE veto regions . . . . .	10
1.17	IceCube alert overview . . . . .	10
2.1	View of Mt. Palomar . . . . .	12
2.2	Schmidt telescope schematic . . . . .	12
2.3	ZTF Field of View . . . . .	13
2.4	CCD operational principle . . . . .	13
2.6	ZTF camera . . . . .	14
2.5	ZTF camera cutaway . . . . .	14
2.7	ZTF filter transmission . . . . .	15
2.8	ZTF field visits . . . . .	15
2.9	ZTF realtime flowchart . . . . .	16
2.10	ZTF flat field illuminator . . . . .	16
2.11	Seeing . . . . .	17
2.12	ZTF image subtraction . . . . .	20
2.13	ZTF subtraction artifact . . . . .	20

# List of Tables





# 1 The IceCube Detector

One of the two most relevant instruments for this thesis is the *IceCube Detector*, a neutrino detector located at the geographic South Pole. It is the successor to the Antarctic Muon And Neutrino Detector Array (AMANDA) at the same location [1, 2].

The basic operational principle of IceCube (and already of AMANDA) is the detection of Cherenkov light within the Antarctic ice. When charged secondary particles created by neutrino interactions travel through the ice, their speed exceeds the phase velocity of light in ice and they emit Cherenkov radiation. The detector consists of 5160 individual digital optical modules (DOMs), buried deep in the ice. These are sensitive to the Cherenkov radiation.

## 1.1 Cherenkov radiation

Cherenkov radiation was first detected in 1934 by Soviet scientist Pavel Cherenkov [4]. It occurs when charged particles travel within a medium with a velocity exceeding the speed of light in that medium. The refractive index in a medium is defined as  $n = \frac{c_0}{c_m}$ , where  $c_m$  is the speed of light in vacuum and  $c_m$  is the phase velocity of light in that medium. Note that the phase velocity of light in a medium can exceed  $c_0$ , so  $n < 1$  is possible.

When charged particles cross an electrically neutral dielectric medium, atoms along the particle's path are briefly polarized and emit electromagnetic radiation.

For slow particles, this radiation destructively interferes with itself, canceling out all signals (see the bottom panel of Fig. 1.1). Now, if the particle is travelling faster than speed of light within the medium  $c_m$ , this destructive interference does not happen. Rather, a cone-shaped wavefront gets created (see top panel of Fig. 1.1). This wavefront constitutes Cherenkov radiation. If the particle has speed  $v = \beta c_0$ , the angle  $\theta$  between the particle trajectory and the direction of the Cherenkov radiation can be calculated as [3]:

[1]: Andrés et al. (1999), *The AMANDA neutrino telescope*

[2]: Andrés et al. (2000), *The AMANDA neutrino telescope: principle of operation and first results*

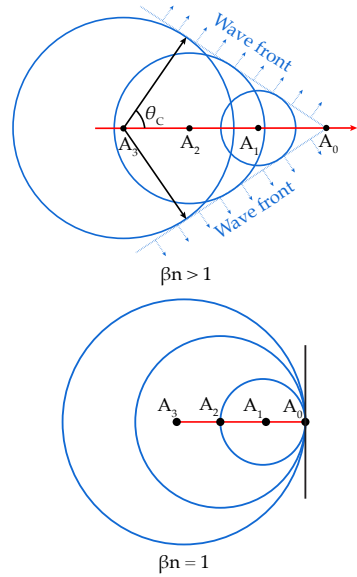


**Figure 1.1:** The principle of Cherenkov radiation. In the upper figure Cherenkov radiation is emitted at the Cherenkov angle  $\theta_C$ , as the radiation emitted at different points in time forms a mutual, cone-shaped wavefront. In the figure on the bottom, all radiation is cancelled out by destructive interference (all circles are subsets of the first on the left, as the particle is not moving faster than light in the medium). Adopted from [3].

[4]: Cherenkov (1934), *Visible emission of clean liquids by action of gamma radiation*

[3]: L'Annunziata (2020), *Handbook of Radioactivity Analysis. Volume 1: Radiation Physics and Detectors*

$$\cos \theta = \frac{\beta}{n} \quad (1.1)$$

1: This is of course rather crude. The  $n$  of Antarctic glacial ice depends e.g. on depth; a fact we will come back to later when discussing directional reconstruction of high-energy IceCube neutrinos.

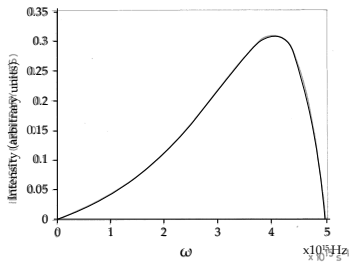


**Figure 1.2:** Cherenkov spectrum for a particle with  $v = 0.8 c_0$  in water. The intensity peaks at  $4 \times 10^{15} \text{ Hz}$ , corresponding to a wavelength of 75 nm, lying at the high-frequency end of the UV spectrum. Adopted from [5].

[5]: Filöp et al. (1992), *Cherenkov radiation spectrum*

[6]: Iams et al. (1935), *The Secondary Emission Phototube*

For example: If the medium is ice, to first order the refractive index  $n \approx 1.31$ .<sup>1</sup> A secondary muon traveling through the ice at  $0.999 c_0$  will therefore emit Cherenkov light at an angle of  $\theta = \cos^{-1} \left( \frac{0.999}{1.31} \right) \approx 40^\circ$ .

Cherenkov radiation does not have spectral peaks, but is continuous, with a relative intensity proportional to the frequency. Note that the refractive index of a medium is also frequency dependent, dropping below 1 in the X-ray. From this it follows that Cherenkov radiation appears blue to the human eye (the high-frequency part dominates) and peaks in the ultra violet (UV), before it sharply drops off in the X-ray regime [5], see Fig. 1.2.

## 1.2 Instrumentation

IceCube detects neutrinos by observing the optical part of their secondary particle Cherenkov spectrum (see section 1.1 above). To understand how this is done, one first needs to look at the working principle of a photomultiplier tube (PMT).

### 1.2.1 Photomultiplier tubes

A PMT is a device used to detect very faint light signals by amplifying them. They consist of vacuum tubes and were successfully realized for the first time in the 1930s [6].

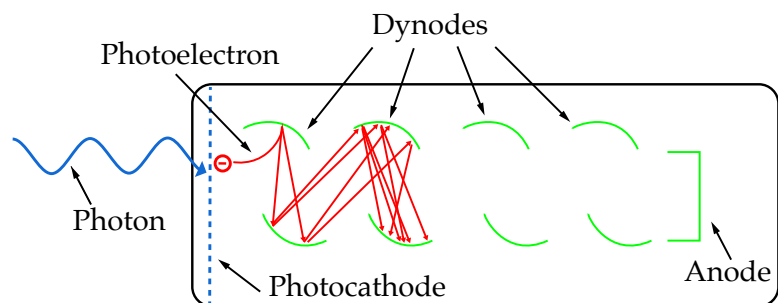


**Figure 1.3:** A photomultiplier tube. Adopted from [7].

[8]: Einstein (1905), *Über einen die Erzeugung und Verwandlung des Lichtes betreffenden heuristischen Gesichtspunkt*

As one can see in Fig. 1.3, there are three principal components: a *cathode*, a number of *dynodes* and an *anode*. When photons hit the cathode, they can release electrons via the photoelectric effect [8]. These photoelectrons are then accelerated (towards the right side in Fig. 1.3) by an electric field within the tube. This field is generated by applying a high voltage between the cathode and the anode.

To amplify the signal, a number of dynodes is placed in between. These are additional electrodes with subsequently higher voltages. When the photoelectron hits the first dynode, a number of secondary electrons are generated, which are then accelerated towards the next dynode by the electric field. This process repeats for every dynode, generating an avalanche of electrons exponentially amplifying the original single

photoelectron signal. The number of secondary electrons hitting the anode is proportional to the number of incident photons, resulting in a linear detector response (as long as the detector stays below its saturation level) [9].

IceCube uses PMTs made by Hamamatsu Photonics (R7081-02), sensitive to photons between 300 nm and 650 nm. They have a quantum efficiency at 390 nm of 25%, are operated with a voltage of 1500 V and have a gain of  $10^7$ . The photon-sensitive surface area is typically  $530 \text{ cm}^2$  [10].

## 1.2.2 The Digital Optical Module

The individual IceCube PMTs for detecting the Cherenkov radiation are enclosed in *digital optical modules* (DOMs). Each DOM consists of a pressure-resistant glass sphere, several controller boards and the PMT, facing downward (see Fig. 1.4). The glass sphere can withstand long-term pressure of 250 bar. The optical transmission of the spheres was measured to be 93% at 400 nm, decreasing to 10% at 315 nm.

The circular main board hosts data acquisition and control, as well as units for communication, calibration and a power converter. Another board interfaces with the PMT, while additional boards delay the PMT signals, generate the high voltage current powering the PMT, as well as control calibration light emitting diodes (LEDs) that generate light flashes which can be received by neighboring DOMs for calibration purposes [11].

Because of data storage restrictions, the DOMs only record the full digitized waveform data after a “hit”. A hit is triggered when also DOMs above and below the DOM in question (to be precise, the neighbors and the next-to-nearest neighbors) report a coincident signal above a certain threshold [11]. To fully record the waveform after a hit, there needs to be some kind of buffer. This is realized with the delay board, which routes the analog PMT signal through a 10 m long, serpentine copper trace to delay it by 75 nm.

The digitization of the PMT waveform is done with the Analog Transient Waveform Digitizer (ATWD), a custom-built application specific integrated circuit (ASIC). Usually lying dormant, the ATWDs start to capture the delayed waveform when the PMT discriminator initiates it. The captured waveforms are only digitized in case a hit (i.e. local coincidence) is registered [12].

The DOMs are connected to the IceCube Laboratory (ICL) with twisted-pair copper cables. The power for the DOM is also transmitted with this cable. Two DOMs share one twisted-pair cable, and each DOM is also directly connected to its two neighbors on the same string (to detect hits, i.e. locally coincident signals). Fig. 1.5 shows the connection layout.

The flasher board houses 12 LEDs operating at  $\sim 400$  nm wavelength. These are used to verify the DOM timing response, to measure the DOM in-ice position, to determine the optical properties of the ice, and to verify the reconstruction algorithms [11].

[9]: Wright (2017), *The Photomultiplier Handbook*

[10]: Abbasi et al. (2010), *Calibration and characterization of the IceCube photomultiplier tube*

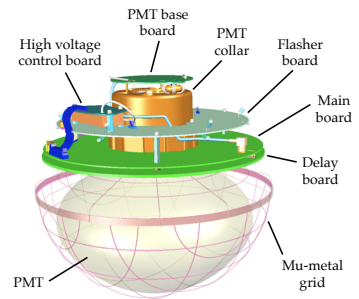


Figure 1.4: The IceCube DOM seen from the side. The detecting side of the PMT is facing downwards, with the main board on the PMT base board on top. From [11].

[11]: Aartsen et al. (2017), *The IceCube Neutrino Observatory: instrumentation and online systems*

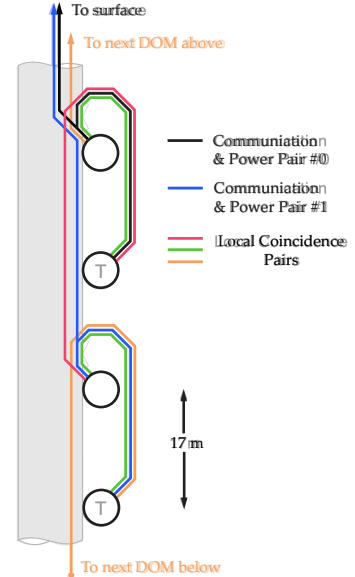
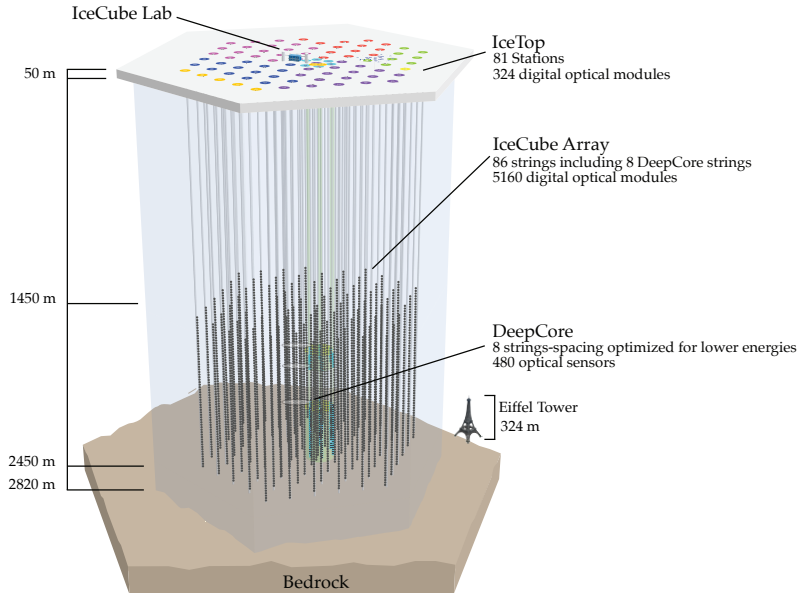


Figure 1.5: Connection scheme for four IceCube DOMs along one string. Pairs of DOMs share one twisted-pair cable. Also, each DOM is directly connected to its direct neighbor above and below. Adopted from [11].

[12]: Abbasi et al. (2013), *IceTop: The surface component of IceCube*



**Figure 1.6:** Side view of the IceCube detector, showing the instrumented array deep in the Antarctic glacial ice. In the center on top is the IceCube Laboratory, where data acquisition takes place. From [13].

### 1.2.3 Detector layout

In total, approximately 5800 DOM units were built and tested, 300 failing tests and the rest being delivered to the South Pole. The vast majority of these were ultimately deployed (5160 in total). The final detector layout (since the last drilling campaign 2010/2011, see below) consists of 86 strings. The DOMs were deployed along those strings, like pearls on a necklace. Each string contains 60 DOMs, with an average horizontal spacing between strings of 125 m [11].

The instrumented part of the strings starts at 1450 m below surface, with one DOM every 17 m to a depth of 2450 m, just above the bedrock at a depth of 2820 m. In Fig. 1.6 the layout of the in-ice array can be seen. The strings follow a roughly hexagonal layout (see Fig. 1.7), with a side length of 1 km<sup>2</sup>. The total instrumented volume of glacial ice is thus 1 km<sup>3</sup> [11]. Of the 5160 deployed DOMs, 92 are dead as of March 2023, a loss of 1.7%<sup>2</sup>.

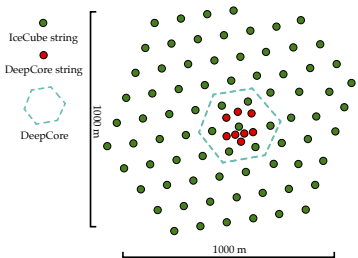


**Figure 1.7:** Top-down view of the IceCube detector, spanning 1 km<sup>2</sup> on the surface. From [13].

2: This is better than the predicted failure percentage, which was projected to be 2% by 2023 [11].

#### DeepCore

3: The hole diameter was larger than the DOM diameter (35 cm) to account for partial refreezing of the bore hole.

### 1.2.4 Deployment

As one can imagine, embedding the DOMs within the ice was a non-trivial task. It required drilling 86 boreholes with a diameter<sup>3</sup> of roughly 60 cm and a length of 2500 m. This was achieved over several drilling campaigns with the Enhanced Hot Water Drill (EHWD) specifically built for this task. This drill had a total power of 5 MW and was able to drill with a maximum speed of 2.2 m min<sup>-1</sup>. With these performance characteristics, one hole was drilled every 48 h on average [11] (drill operation happened around the clock). It took 7 drilling seasons to deploy the final IceCube86 setup, from the Antarctic summers 2004/2005 to 2010/2011. Fig. 1.8 shows the tower operations site directly above the bore hole [14].

The water for drilling the holes was heated to 88 °C with 35 water heaters working in parallel, each providing 125 kW power. The average amount of fuel used per drill hole was 27 000 L [14].

[14]: Benson et al. (2014), *IceCube Enhanced Hot Water Drill functional description*

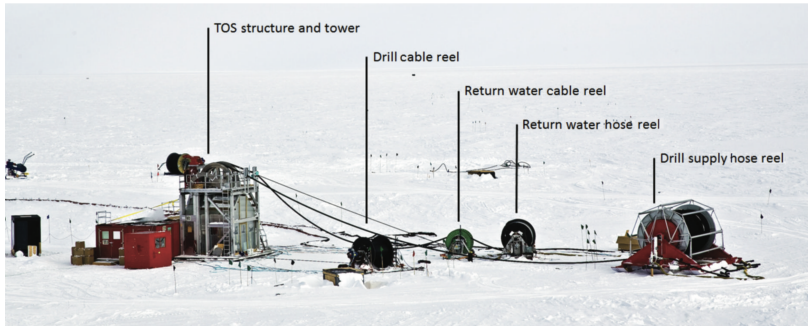


**Figure 1.8:** The hole drilling part of the IceCube Enhanced Hot Water Drill, excluding the hot, pressurized water supply. One can see the tower operations site (TOS) above the hole and the hoses providing hot water and returning cooled water from the bore hole to the generators in a closed loop. From [14].

## 1.2.5 The IceTop surface array

One of the major classes of background events are cosmic ray interactions in the atmosphere, as the muons generated in these are indiscernible from neutrino-induced muons within the in-ice array (see section 1.4.1). IceTop serves as a partial veto against these, as it is sensitive to the airshowers from which atmospheric muons and neutrinos stem.

The IceTop surface array consists of  $2 \times 81$  ice-filled Cherenkov tanks. These are placed in pairs on the same hexagonal grid as the DOM strings for the in-ice array. Each tank is equipped with two IceCube DOMs (see section 1.2.2) [12].

## 1.2.6 Data acquisition

As noted above, only for locally coincident hits in multiple detectors the full waveforms are digitized by the DOMs. These are then sent to the IceCube Laboratory on the surface via the twisted-pair cable datalink, where all DOM data is ingested into the data acquisition system (DAQ). Hits throughout the detector are investigated by the system to establish common causality by temporal and sometimes spatial patterns. All hits for which common causality can be established form an *event*. The rate of these events varies seasonally with the atmospheric muon flux, with a median event rate of 2.7 kHz and a total data rate of  $1 \text{ TB d}^{-1}$  (roughly  $100 \text{ Mbit s}^{-1}$ ) [11].

As satellite bandwidth is limited and costly, further software triggers on-site reduce the data rate to 15% of the initial rate. These events are then transmitted via satellite to the IceCube data center at the University of Wisconsin-Madison for further analysis. The full event stream is also written to redundant disks, which are transferred twice per year to Madison.

## 1.2.7 Time synchronization

As timing information is crucial for event constitution and reconstruction (more on that later), all DOMs need to be synced to a common clock. This is achieved by syncing the whole system to a Symmetricom ET6000 GPS receiver. The synchronization of individual DOMs is performed while data transfer is paused.

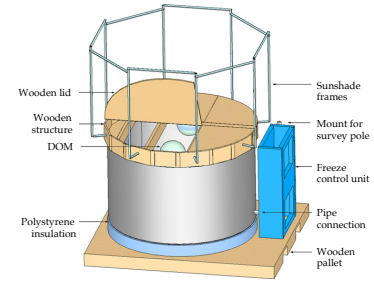


**Figure 1.9:** IceTop surface Cherenkov detector tank. From [12].

more detail

This is achieved with Reciprocal Active Pulsing (RAPcal): A bipolar pulse is initiated on the surface and sent to the DOM. The sender saves the local time when it sends the pulse and starts a timer. Upon reception down the string, the DOM also saves its current local time, saves the received pulse waveform, starts a timer, responds with a bipolar pulse of its own and stops the timer. Upon reception, the surface station stops its timer and requests the received pulse waveform and all timing information from the DOM.

With these six pieces of information – the two transmit timestamps, the two receive timestamps and both waveforms – a transformation from the GPS-synchronized surface to local DOM time domain and vice versa can be calculated, with a precision of 1–2 ns [15].

[15]: Abbasi et al. (2009), *The IceCube data acquisition system: Signal capture, digitization, and timestamping*

## 1.3 Angular Reconstruction

The goal of IceCube reconstruction is twofold: Reconstructing the deposited neutrino energy, and reconstructing the neutrino arrival direction. These two goals are somewhat mutually exclusive, which is reflected by broadly classifying the events seen by the detector in two categories: *Track events* and *cascade events*.

### 1.3.1 Event types

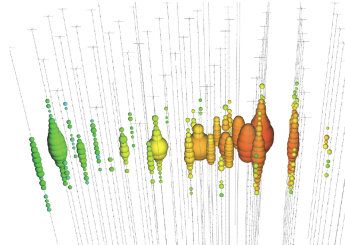


**Figure 1.10:** Cascade event: The long track allows for good angular reconstruction, with high uncertainty on the event energy. From [masterclass.icecube.wisc.edu](http://masterclass.icecube.wisc.edu).

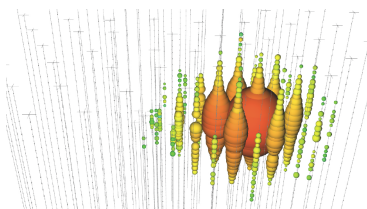


**Figure 1.11:** Cascade event: The energy is fully contained in the detector, as the event is relatively isotropic. The angular uncertainty is quite large though. From [masterclass.icecube.wisc.edu](http://masterclass.icecube.wisc.edu).

ref to theory section

[16]: R. Abbasi et al. (2022), *Evidence for neutrino emission from the nearby active galaxy NGC 1068*

[17]: Aartsen et al. (2017), *The IceCube realtime alert system*

[18]: Ahrens et al. (2004), *Muon track reconstruction and data selection techniques in AMANDA*

Track events (Fig. 1.10) are produced by secondary muons resulting from the charged-current interaction of muon neutrinos with Antarctic glacial ice. They leave tracks in the ice with a length on the order of kilometers. This allows for a good angular resolution, ranging from  $1^\circ$  for a 1 TeV muon to  $0.3^\circ$  for a 1 PeV muon [16]. The drawback is a large energy uncertainty, as part of the muon track can lie outside the instrumented volume [17].

Cascade events (Fig. 1.11) on the other hand are initiated by the charged-current interactions of  $\nu_e$  and  $\nu_\tau$ , as well as by neutral-current interactions from neutrinos of all flavors. They are usually relatively isotropic and contained within a small fraction of the detector, as typical track lengths are of  $\mathcal{O}(10\text{ m})$ . Their relative isotropy only allows for poor angular resolution ( $10\text{--}15^\circ$ ), but comparably good energy reconstruction ( $\frac{\delta E}{E} \approx 15\%$ ) [17].

As this thesis is mainly interested in the sources of high-energy astrophysical neutrinos, the track events are more important, and I will focus on the angular reconstruction of those.

### 1.3.2 Likelihood approach

The basic angular reconstruction algorithm for muon tracks used in IceCube is based on the work done for AMANDA. It is based on a maximum-likelihood method [18]. This can be understood as follows: Given a set of unknown track parameters  $\vec{a}$  and a set of experimentally determined values  $\vec{x}$ , what values of the unknown parameters do

maximize the probability of measuring the actually observed values of  $\vec{x}$ ?

This likelihood is denoted  $\mathcal{L}(\vec{x}|\vec{a})$ . If the components  $x_i$  of  $\vec{x}$  are independent, it can be expressed as

$$\mathcal{L} = \prod_i p(x_i|\vec{a}) \quad (1.2)$$

Here,  $p(x_i|\vec{a})$  is the probability density function (PDF) of measuring  $x_i$  given a set of parameters  $\vec{a}$ . Maximizing  $\mathcal{L}$  when varying  $\vec{a}$  (or, for technical reasons, minimizing  $-\log \mathcal{L}$ ) results in the most likely set of unknown parameters  $\vec{a}$ , and we are done with the reconstruction.

## Parametrization

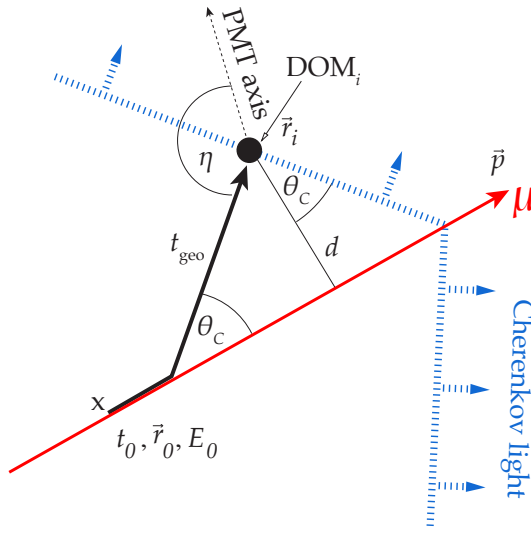


**Figure 1.12:** Parametrization for the angular muon reconstruction. Adopted from [18].

To simplify matters, we assume that we are dealing with a muon with maximum allowed speed ( $\beta = 1$ ), travelling along a track of infinite length. Furthermore, we neglect stochastic photon losses. The set of parameters  $\vec{a}$  needed to describe the physical situation in the detector are visualized in Fig. 1.12:  $\vec{a} = (t_0, E_0, \vec{r}_0, \vec{p})$ . They describe the trajectory of a muon at time  $t_0$  with energy  $E_0$  at position  $\vec{r}_0$ , traveling in the direction  $\vec{p}$ . So we are dealing with one time parameter, one energy parameter and positional parameters in 5 dimensions, where the vertex position  $\vec{r}_0$  can be expressed in (x,y,z) and the muon direction  $\vec{p}$  is usually described by two angles, zenith and azimuth.

Now, a DOM in the detector at position  $\vec{r}_i$  with a distance  $d$  to the track can be hit by Cherenkov photons emitted by the muon along the track with the Cherenkov angle  $\theta_C$ , arriving at an angle  $\eta$  with respect to the PMT axis. Without scattering, the photon reaches the DOM<sub>i</sub> at the geometrical time  $t_{\text{geo}}$ , which can be expressed as follows:

$$t_{\text{geo}} = t_0 + \frac{|\vec{p} \cdot (\vec{r}_i - \vec{r}_0)| + d \cdot \tan \theta_C}{c_0} \quad (1.3)$$

with  $c_0$  the vacuum speed of light. As this does not take scattering into account, it is useful to define a relative time of arrival, the *time residual*  $t_{\text{res}} = t_{\text{hit}} - t_{\text{geo}}$ . This is the additional time introduced by scattering as opposed to a Cherenkov photon travelling directly from the muon to the DOM.

As  $t_{\text{res}}$  is the most significant observable for each DOM, we can simplify  $x_i$  to  $t_{\text{res},i}$ , and express  $\vec{a}$  as a function of the individual DOM parameters:  $\vec{a} = (d_i, \eta_i, \dots)$ .

### 1.3.3 Single photoelectron fit

Matters can be simplified further. While the muon is travelling and emitting Cherenkov light, multiple photons can hit each DOM. One simplification is to only regard the *first* photon hitting an individual DOM, as it is usually less scattered than the average photon. If the reconstruction is carried out with this simplification, it is called *single photoelectron* (SPE) fit. The likelihood function for this is:<sup>4</sup>

$$\mathcal{L}_{\text{SPE}} = \prod_i^{\text{1st hits}} p(t_{\text{res},i} | \vec{a} = d_i, \eta_i, \dots) \quad (1.4)$$

where the probability density function  $p(t_{\text{res},i} | \vec{a})$  is obtained from simulations modeling the photon propagation through the Antarctic ice.

### 1.3.4 Multi photoelectron fit

A complication is that one would expect the first photon in a DOM detecting multiple photons *earlier* than a photon detected by a DOM only registering this very single photon. This leads to the *multi photoelectron* (MPE) fit. Here, the single photon part of the likelihood is modified by the cumulative PDF (CDF), which is given by

$$P(t_{\text{res},i} | \vec{a}) = \int_{t_{\text{res},i}}^{\infty} p(t | \vec{a}) dt \quad (1.5)$$

Using this, the MPE likelihood is given as

$$\mathcal{L}_{\text{MPE}} = \prod_i^{\text{1st hits}} p(t_{\text{res},i} | \vec{a}) \cdot N_i \cdot (1 - P(t_{\text{res},i} | \vec{a}))^{N_i - 1} \quad (1.6)$$

where  $N_i$  is the total number of photons recorded by DOM <sub>$i$</sub>  [18].

## 1.4 The Realtime Alert Program

Since 2016, IceCube is hosting a realtime alert program, providing the astrophysical community with low-latency, high-quality astrophysical neutrino alerts [17]. This program saw a major revision in 2019, when two new alert streams, namely *Gold* and *Bronze*, were created [19]. As all alerts used within this work except one stem from this revised system, I will focus on presenting the newer alert scheme.

[19]: Tung et al. (2019), *The Next Generation of IceCube Real-time Neutrino Alerts*

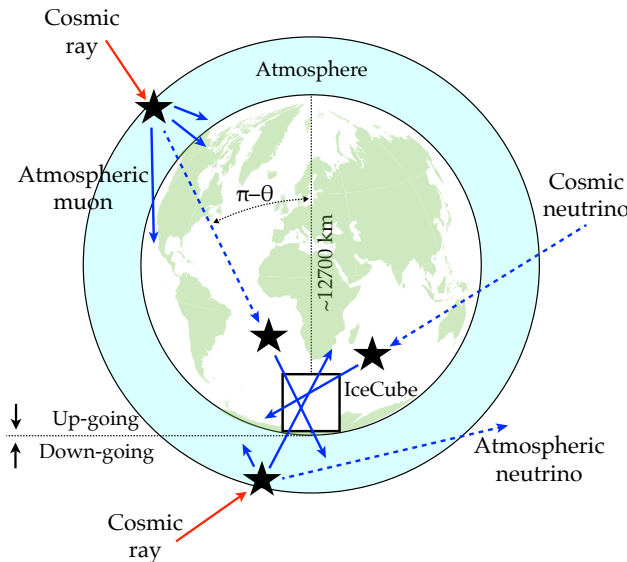


**Figure 1.13:** Background events in the detector. Cosmic rays hit the atmosphere around the globe and produce muons (solid blue arrows), as well as neutrinos (dashed blue arrows). When constraining to *up-going* events from the northern hemisphere, the detector is shielded from atmospheric muons, but not atmospheric neutrinos, as these can traverse the earth. Adopted from [13].

## 1.4.1 Background

Depending on the declination, there are two major sources of background events in the IceCube detector, both stemming from secondary cosmic ray particles from the earth's atmosphere.

**Atmospheric muons** are created by cosmic rays hitting the atmosphere. One can efficiently filter this background by restricting the analysis to *up-going* muon tracks. These are tracks that come from the bottom of the detector, i.e. the northern hemisphere. Atmospheric muons stemming from cosmic ray events in the northern hemisphere are filtered out by the earth's core (see Fig. 1.13), as the mean free path of muons within the earth is much smaller [20] than the distance they have to cross (see Fig. 1.14). Note that due to light scattering within the ice, some down-going tracks can be misclassified as up-going [13].

One complication here stems from the fact that the earth starts to become opaque for neutrinos of higher energies. Studies interested in PeV neutrinos therefore must deal with the fact that these are the more suppressed the longer their path through the earth is. E.g. a 1 PeV neutrino with a zenith angle of  $140^\circ$  is absorbed with 90% probability [21].

**Atmospheric neutrinos** also stem from cosmic ray showers. These are harder to suppress by directional cuts, creating an irreducible background: When atmospheric neutrinos cross the earth and interact with the matter close to the detector, they can produce muons indistinguishable from muons created by 'proper' cosmic neutrinos [13].

## 1.4.2 Event selection

Gold and bronze alerts are drawn from three different selection schemes, originally designed to cater to different science goals. These are **High Energy Starting Events** (HESE), **Extremely High Energy** (EHE) events and **Gamma-Ray Follow Up** (GFU) events.

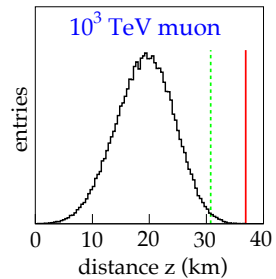


**Figure 1.14:** Free path length for 1 PeV muons in ice. Note that the mean free path in ice is slightly longer than in rock. From [20].

[20]: Chirkin et al. (2004), *Propagating leptons through matter with Muon Monte Carlo (MMC)*

[13]: Ahlers et al. (2018), *Probing particle physics with IceCube*

[21]: Aartsen et al. (2017), *Measurement of the multi-TeV neutrino interaction cross-section with IceCube using Earth absorption*

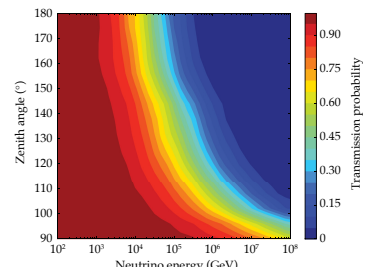


**Figure 1.15:** Neutrino transmission probability through the earth. The longer the distance travelled (higher zenith angles) and the higher the neutrino energy, the more likely is absorption. From [21].

[22]: Aartsen et al. (2013), *Evidence for High-Energy Extraterrestrial Neutrinos at the IceCube Detector*

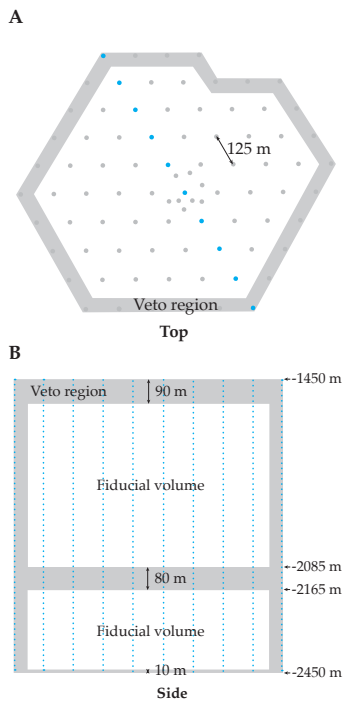


**Figure 1.16:** High-energy starting events veto regions. The strings marked in blue in the top-down view at the top (A) show the location of the side view, displayed at the bottom (B). From [22].

**HESE** are events that start *within* the detector. This is guaranteed by using the outer regions of the detector as a veto region, in which (almost) no Cherenkov light must be detected [22]. The sizes of those regions can be seen in Fig. 1.16. The majority of these events are cascades and therefore not well suited for observational follow-up. Because of this, additional cuts are applied: The reconstruction must favor a track interpretation of the event, and the reconstructed track length must exceed 200 m [19].

**EHE** events must contain at least 4000 photoelectrons, aiming at neutrino energies of 0.5–10 PeV. Additionally, a  $\chi^2$ -based goodness-of-fit cut is applied to select track-like events with good reconstructions. Lastly, a cut depending on the zenith angle is also applied on the number of photoelectrons required [19].

**GFU** events are selected based on a boosted decision tree trained to identify *through-going* (as opposed to ‘starting’) track events with astrophysical origin. Energy cuts are applied: Northern hemisphere (up-going) events are selected based on their reconstructed muon energies, while southern hemisphere (down-going) events are selected based on the total photoelectron charge deposited in the detector.

The cuts from all three event pools are gauged to achieve two different values of *signalness*, which is a proxy for the probability that the event is of astrophysical origin [19]. It is defined as follows:

$$\text{Definition 1.4.1} \quad \text{Signalness}(E, \theta_{\text{zen}}) = \frac{N_{\text{signal}}(E, \theta_{\text{zen}})}{N_{\text{signal}}(E, \theta_{\text{zen}}) + N_{\text{background}}(E, \theta_{\text{zen}})}$$

where  $\theta_{\text{zen}}$  is the zenith angle and  $E$  is the respective energy proxy of the event selections described above.

The cuts on the individual event selections are tuned to ensure that *gold* alerts on average have a signalness  $> 50\%$ , and *bronze* alerts have a signalness  $> 30\%$ .

### 1.4.3 Alert distribution

All events that pass a first stage of filtering are sent to the IceCube data center (see section 1.2.6) via Iridium satellite to minimize latency. There, their signalness is computed. If they make either the gold or the bronze selection, they are distributed globally with the Gamma-Ray Coordinates Network (GCN) in the form of GCN Notices.

Each notices contains the discovery time, a unique event number, the reconstructed direction in right ascension (RA) and declination (Dec) of the candidate neutrino, a statistical error for the direction, the reconstructed neutrino energy, the signalness and the false alarm rate [19].

Those information are later appended by a computationally more demanding, but more sophisticated reconstruction, which is initiated manually. These are typically distributed a few hours after the initial notice in the form of a GCN circular [19].

As of March 2023, a total of 106 events have been distributed in this format, with 7 later being retracted. As the gold/bronze alert stream started in June 2019, this amounts to 2.2 non-retracted alerts per month<sup>5</sup> (0.8 gold alerts, 1.4 bronze alerts).

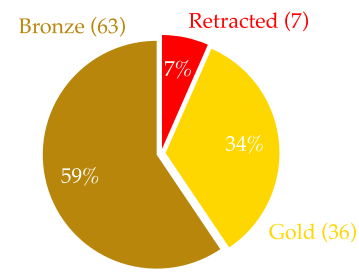


**Figure 1.17:** High-energy neutrino alerts issued by IceCube since start of the new alert stream in June 2019.

5: This is slightly below the 2.5 alerts per month predicted in [19].



## 2 The Zwicky Transient Facility

The second instrument relevant for this thesis is the Zwicky Transient Facility (ZTF). It is named after the notorious Swiss-American astronomer Fritz Zwicky, who e.g. first employed the Virial theorem to infer the existence of dark matter [23]. Furthermore, together with Walter Baade, he posited the existence of supernovae and the creation of neutron stars in such events [24].

ZTF is a wide-field optical survey telescope. This means that it normally operates by scanning the full sky with a fixed cadence, in contrast to pointing to specific objects. It is located at Mount Palomar in California, United States, at 1700 m above sea level, roughly 130 km southeast of Los Angeles. Its optical system, the 1.2 m (48 inch) Samuel Oschin telescope, is a Schmidt design (see below) and was inaugurated in 1948 [25]. At the time of inauguration and for years to come, it was the largest Schmidt telescope in the world. Originally, the telescope used photographic plates, covering a field of view (FoV) of  $44 \text{ deg}^2$ . As such photographic plates have obvious drawbacks, and because technological progress made it possible, the Near-Earth Asteroid Tracking (NEAT) program [26] replaced them with a charge-coupled device (CCD) camera in the early 2000s.

Over the course of the next years the camera was updated several times. The immediate predecessor of ZTF, the Palomar Transient Factory (PTF) [27], began operation in 2009. Equipped with a 96 Megapixel camera, it already had many of the characteristics of ZTF: A fully automated survey, searching for optical transients with a CCD camera.

PTF's successor in spirit, ZTF, contains the first electronic camera. With  $47 \text{ deg}^2$ , it covers almost the full FoV of the P48. The main design metric for ZTF was *volumetric survey speed*. This is the volume within which an object of given absolute magnitude can be detected in one exposure, divided by the total time for the exposure (observation plus overhead) [28]. The system saw first light in 2017, and started its scientific use in the year after (the first survey data was taken on 2018-03-20). As of writing, ZTF is still operational.

The two other telescopes located on Mount Palomar. The 1.5 m (60 inch) P60 telescope houses the SED Machine (SEDM) [29], a fully robotic, low-

[23]: Zwicky (1933), *Die Rotverschiebung von extragalaktischen Nebeln*

[24]: Baade et al. (1934), *On Super-Novae*

[26]: Pravdo et al. (1999), *The Near-Earth Asteroid Tracking (NEAT) Program: An Automated System for Telescope Control, Wide-Field Imaging, and Object Detection*

See <https://sites.astro.caltech.edu/palomar/about/telescopes/oschin.html> for a historical overview.

[27]: Law et al. (2009), *The Palomar Transient Factory: System Overview, Performance, and First Results*

[28]: Bellm (2016), *Volumetric Survey Speed: A Figure of Merit for Transient Surveys*

[29]: Blagorodnova et al. (2018), *The SED Machine: A Robotic Spectrograph for Fast Transient Classification*



**Figure 2.1:** View of Mt. Palomar with the three telescopes highlighted in the text. Image credit: Caltech, annotations by the author.

resolution spectrograph used for automatic classification of transients. The largest facility on the mountain is the 200-inch (5.1 m) Hale Telescope, which is used for optical and infrared photometry as well as mid- and high-resolution spectroscopy of fainter sources. Together, these telescopes form a natural hierarchy: ZTF is the discovery engine for optical transients. Promising sources are then classified with SEDM. If sources warrant it, deeper photometry and higher resolved spectroscopy can then be obtained with the big gun, the P200. All three telescopes are shown in Fig. 2.1.

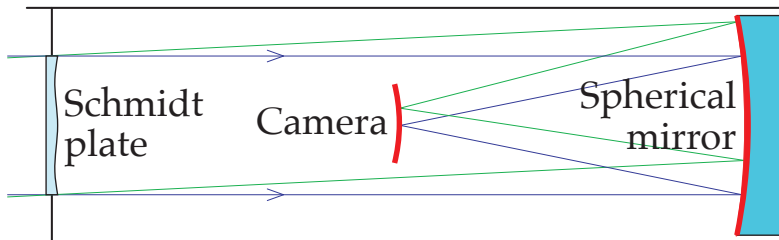
## 2.1 Telescope Design

[30]: Schmidt (1938), *Ein lichtstarkes komafreies Spiegelsystem*

A *Schmidt telescope* is by design dedicated to taking images, contrary to earlier designs allowing actually looking through an eyepiece [30]. For this reason, it is also referred to as a *Schmidt camera*. The design goal is a wide FoV. This makes it the ideal instrument for sky surveys, where a large FoV maximizes the on-sky area that can be monitored. A Schmidt telescope combines a spherical mirror at the end of the telescope tube with an aspherical correcting lens (Schmidt plate) at the tube's entrance. The use of a spherical mirror combined with the correcting lens gets entirely rid of comatic aberration.

[31]: Cannon (1995), *Schmidt Telescopes: Their Past, Present and Future*

**Figure 2.2:** Schmidt telescope schematic. Light enters from the left, passes the Schmidt plate (an aspherical correcting lens), gets reflected by a spherical mirror at the end onto a photographic plate or camera halfway down the tube. Figure adopted from <https://commons.wikimedia.org/wiki/File:Schmidt-Teleskop.svg>.



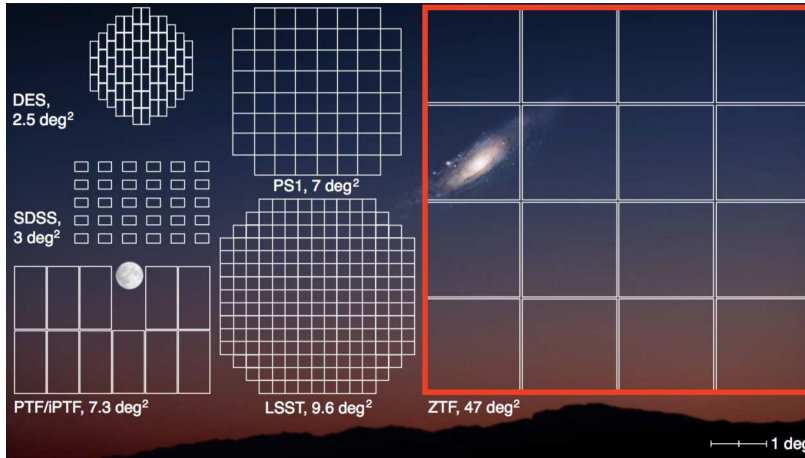


**Figure 2.3:** ZTF field of view (highlighted in red) in comparison to other sky survey telescopes, including the future Rubin observatory (LSST). Note also the 6.5-fold increase with respect to ZTF's predecessor, PTF/iPTF. From [34], highlighting by the author.

them were space telescopes: ESA's astrometry mission *HIPPARCOS* [32] (1989–1993) and the NASA exoplanet mission *Kepler* [33] (2009–2018). In both cases, the mission entailed monitoring of large areas of the sky; prime territory for Schmidt telescopes.

[32]: (1997), *The HIPPARCOS and TYCHO catalogues. Astrometric and photometric star catalogues derived from the ESA HIPPARCOS Space Astrometry Mission*

[33]: Koch et al. (2010), *Kepler Mission Design, Realized Photometric Performance, and Early Science*

## 2.2 Camera

The ZTF camera is a CCD design, consisting of 16 individual CCDs by commercial manufacturer e2v (now Teledyne, *Science CCD 231-C6*), each having  $6144 \times 6160$  pixels, resulting in a total camera resolution of  $\sim 600$  Megapixel [35]. As one can see in Fig. 2.6, the array of 16 CCDs is slightly bent. This is necessitated by the Schmidt design, where the camera needs to be spherical, matching the spherical mirror. As individual CCDs are flat, each of the 16 sensors is installed slightly tilted, tracing the overall curvature. To get rid of residual deviations from the global curvature, in front of each sensor a field flattener lens is mounted [36].

[35]: Dekany et al. (2016), *The Zwicky Transient Facility Camera*

### CCDs

CCDs are silicon-based light sensors. They consist of arrays of coupled metal-oxide semiconductor (MOS) capacitors, each one able to store the charge created by incident photons; one capacitor per pixel of the sensor array. The array is exposed to light for an amount of time (exposure time). During the exposure, incident photons create a charge proportional to the amount of light hitting each capacitor via the photo-electric effect. This charge is accumulated in each capacitor until the exposure is finished. To read out the CCD, the charges need to be moved to neighboring capacitors. When the MOS capacitors are tightly placed, one can move the charges from one capacitor to the next by changing the voltages on the capacitor's gates.

[36]: Bellm et al. (2019), *The Zwicky Transient Facility: System Overview, Performance, and First Results*

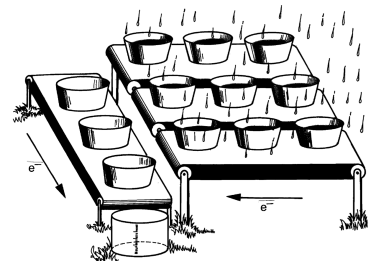


**Figure 2.4:** CCD operational principle, explained with buckets measuring precipitation. From [37].

In Fig. 2.4 the principle of a CCD is explained with little buckets collecting rain water. Each bucket symbolizes one capacitor or one pixel of the sensor array respectively. After the rain has stopped (the exposure is finished), each bucket naturally contains an amount of water proportional to the amount of water that rained down over it. Now the amount of

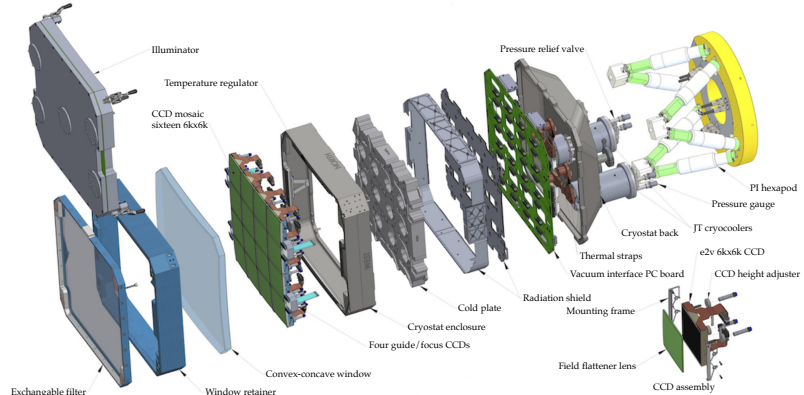


**Figure 2.6:** The ZTF camera. One can see the CCDs sandwiched between the filter on the front and the cryostat on the back. From [36].

water in each bucket (the charge deposited by incident light in each capacitor) needs to be measured.

To do this, the buckets in each row are moved one position to the left with horizontal conveyor belts. Each bucket at the left end of the horizontal conveyor belt is then emptied into the bucket on the single vertical conveyor belt. The buckets of this vertical belt are then one by one drained into the measuring bucket on the bottom left. After all buckets on the vertical belt are emptied, the process starts anew, until all buckets are empty. As one can see, the time this process takes scales linearly with the amount of buckets (or pixels) [37]. To speed up the process, one can subdivide the sensor area into smaller sections, which are read out in parallel.

The typical exposure for the ZTF camera is 30 s, while the readout time (emptying and measuring the charges in each capacitor) takes 8.2 s. Readout and digitization is done in parallel for four quadrants, each containing 4 CCDs. The four readout devices for the quadrants are *Archon* CCD controllers by Semiconductor Technology Associates (STA). Each of these operates 16 simultaneous readout channels, four for each CCD. In summary, the camera is read out simultaneously in 64 independent regions to speed up the process.

An additional four smaller CCDs (2k x 2k pixels) are used as guidance, tip, tilt and focus sensors, with one additional Archon controller to read out these sensors [38]. To lower the thermal noise of the camera, it is placed on top of a cryostat cooling the CCDs to 160 K [35].

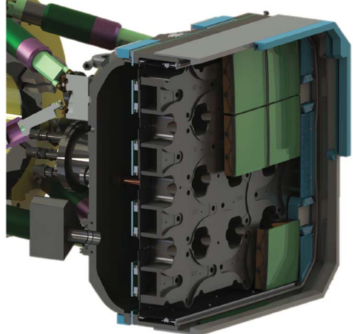


**Figure 2.5:** The ZTF camera in detail. From [38].

[37]: Janesick et al. (1987), *Scientific Charge-Coupled Devices*

[38]: Dekany et al. (2020), *The Zwicky Transient Facility: Observing System*

## 2.3 Optical System

### Filters and shutter

As the CCDs of the camera cannot “see” color, different filters need to be put in front of the camera to obtain color information. With ZTF, there are three different filters available: A *g*-band filter with a median wavelength of 472 nm (corresponding to blue light), an *r*-band filter (median wavelength: 634 nm, red light) and an *i*-band filter (789 nm, near-infrared). These filters can be changed with a robotic arm, securely stowing the replaced filter and magnetically attaching the new one [38]. This process takes 110 s [36].

The main decision goal for the filter selection was to maximize signal-to-noise ratio by avoiding major sky emission lines at Mt. Palomar while avoiding excessive costs. ZTF does not exactly match the filters of potential calibrators, e.g. the Sloan Digital Sky Survey (SDSS) [39], PanSTARRS (PS1) [40] or *Gaia* [41]. This was justified with the overall different telescope design of ZTF [36].

The transmission of each filter and the CCD quantum efficiency curve can be seen in Fig. 2.7. As one can see, the quantum efficiency starts to decrease within the *r*-band towards higher wavelengths, rendering the *i*-band the least sensitive of the three filters. The  $5\sigma$  median sensitivity for a 30s exposure reflects that fact. It is 20.8 (21.1) mag in the *g*-band, 20.6 (20.9) mag in the *r*-band and 19.9 (20.2) mag in the *i*-band; with values for optimal conditions (new moon) in brackets. The resulting median image quality is 2.1" (*g*-band), 2.0" (*r*-band) and 2.1" full width at half maximum (FWHM) of the point spread function (PSF, see PSF photometry section below) [36].

To decrease light obstruction, the ZTF shutter was newly developed and is mounted in front of the aperture, outside of the telescope tube. It was developed by Deutsches Elektronen-Synchrotron (DESY) in cooperation with industry partner Bonn-Shutter and allows to open and close in 290 ms [38].

## ZTF grid

One exposure during regular operations – in contrast to e.g. deep target of opportunity (ToO) images – lasts 30 s. There is an additional  $\sim$ 15 s overhead for readout and slewing the telescope. Also some additional time is needed to exchange the filters. Therefore, a typical night lasting 8.67 h [42] results in roughly 700 exposures. In total, these amount to a sky area of over 32 500 deg<sup>2</sup>, allowing to cover the full visible sky at Mount Palomar 15° above the horizon at least once.

To aid in the robotic operation and to simplify matters, ZTF operates on a fixed primary on-sky grid of so-called “fields”. Each field corresponds to a fixed sky location with an area of 47 deg<sup>2</sup>, and the telescope is exclusively pointing to those fields. Note that with such a system, some parts of the sky will always fall into the chip gaps (the parts of the FoV that fall between the 16 CCDs). To mitigate that, there exists a *secondary grid* that is diagonally offset from the primary grid. Fig. 2.8 shows the primary grid and the number of visits per field in the *g*-band during the first week of May 2020.

## 2.4 Calibration and Image Processing

The ZTF image processing can be divided into two parts: Creation of the science exposures takes places locally at Mount Palomar, while calibration, creation of the final data products, extraction of transients and archival storage happens at the Infrared Processing and Analysis Center (IPAC)<sup>1</sup> situated on the campus of the California Institute of Technology (Caltech). IPAC ultimately hosts the ZTF images as part of IRSA<sup>2</sup>, the Infrared Science Archive.

[39]: York et al. (2000), *The Sloan Digital Sky Survey: Technical Summary*

[40]: Kaiser et al. (2002), *Pan-STARRS: A Large Synoptic Survey Telescope Array*

[41]: Prusti et al. (2016), *The GAIA mission*

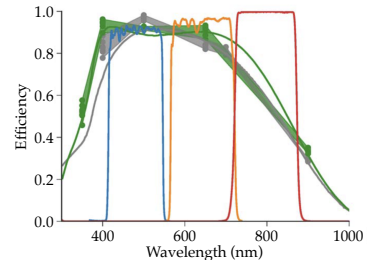


**Figure 2.7:** ZTF filter transmission for the three different bands (*g*-band: blue, *r*-band: orange, *i*-band: red). The green and gray datapoints show the CCD quantum efficiency measurements (single and double-layer reflective coating). From [36].

[42]: Masci et al. (2019), *The Zwicky Transient Facility: Data Processing, Products, and Archive*

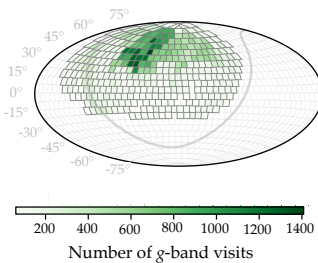


**Figure 2.8:** Number of ZTF *g*-band field visits during the first week of May 2020. The primary grid fully tiles the sky accessible at Mount Palomar.

1: <https://www.ipac.caltech.edu>

2: <https://irsa.ipac.caltech.edu>

The full calibration and image processing pipeline is shown in Fig. 2.9. First come the different calibration steps: overscan and bias correction, flat fielding, as well as astrometric and photometric calibration. This is followed by creating the difference images and finally extracting the sources. I will briefly explain the different steps in the next sections.

## On-site processing and datalink

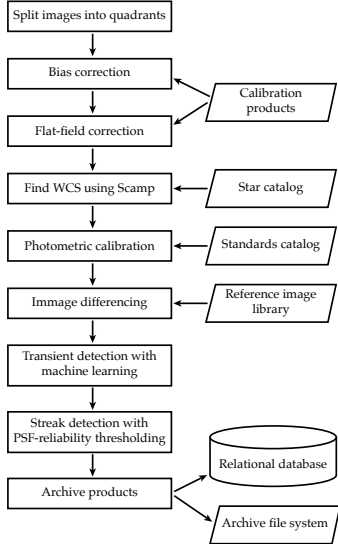


**Figure 2.9:** Flowchart of the ZTF calibration, starting with the raw images on the top and ending with the final science products on the bottom. Adopted from [34].

3: <https://hpwren.ucsd.edu/>

Each image taken on site (calibration and science exposures alike) is stored as FITS file and subsequently compressed losslessly. The compressed images on average use 5bit per pixel, so the full image is roughly 380 MB large. These images are immediately sent to IPAC with the High Performance Wireless Research & Educational Network (HPWREN)<sup>3</sup>, a microwave-based data network, linking Palomar Observatory with the IPAC post-processing site. Each transfer typically takes 20s, keeping up with the pace of ZTF observations [38].

## Overscan correction

As the temperature of the CCDs changes with time, each image is subject to a time-dependent global offset induced by thermal noise. To correct for this, an *overscan* region is used. In the case of the ZTF CCDs, this region does not correspond to physical pixels, but is created during CCD readout. If one reads out more clock cycles than pixels are available, the charge that has gathered during science readout can be accessed. For ZTF, this is done for an additional 24 cycles, corresponding to 24 overscan pixels for each sensor row. After this, the median of these 24 pixels is taken and the full overscan column is fitted with a quadratic function. For each and every image taken by the camera, the bias described by this quadratic function is then subtracted from the image [43].

## Bias correction

[44]: Howell (2006), *Handbook of CCD Astronomy*

The CCD pixels also have different zeropoints. Luckily, this variation has a higher degree of time-stability [44]. To correct it, at the beginning of each night at least 10 so-called *bias* images are taken and overscan corrected. These images are zero-second exposures which are then stacked. After this, the truncated mean of each pixel is calculated, constituting the final bias image for the night (and filter). This bias image is subtracted from each science exposure using the respective filter taken during the night [43].

## Flat fielding

The pixels in the CCDs do not only differ in zero point, they also have slightly different gain or quantum efficiency. This means, their *response* to light is not uniform. To account for this, the calibration needs a structureless, uniformly bright light source against which the individual pixel response can be measured [44]. In the case of ZTF this is achieved by using a flat field illuminator consisting of a round screen illuminated



**Figure 2.10:** The ZTF flat field illuminator. From [38].

by eight identical boards with LEDs, each board housing  $4 \times 15 = 60$  LEDs of 15 different colors, covering the full wavelength region of ZTF [38].

Each afternoon, before science operations begin, at least 20 images per filter are taken of the flat field illuminator. These are then overscan corrected, the bias image is subtracted, and the pixel values are normalized to a truncated global mean of 1 over the image (to allow for later division). After this individual treatment, all flat field images per filter are stacked to a truncated mean per pixel and outlier rejection is applied to isolate additional noisy pixels. All science images taken during the night are divided by this flat field image [43].

## Astrometric calibration

Astrometric calibration is the mapping of image pixel coordinates to an on-sky coordinate system. For ZTF, this is performed with stars contained in the *Gaia* Data Release 1 (*Gaia* DR1, [45]). As it is a mission designated to high-precision astrometry, *Gaia* is the ideal reference for this task. Prior to cuts, the DR1 contains over 1 Billion sources. From these, sources are selected that are neither too faint, nor run risk of saturating the detector ( $12 \leq G \leq 18$  mag). The astrometric solution is derived using the SCAMP [46] package [42]. For this, stars are extracted with SExtractor [47] and matched to the *Gaia* stars. The pointing, rotation and polynomial distortion needed to match the stars constitutes the astrometric solution.

[45]: Brown et al. (2016), *Gaia Data Release 1. Summary of the astrometric, photometric, and survey properties*

[46]: Bertin (2006), *Automatic Astrometric and Photometric Calibration with SCAMP*  
[42]: Masci et al. (2019), *The Zwicky Transient Facility: Data Processing, Products, and Archive*

[47]: Bertin et al. (1996), *SExtractor: Software for source extraction*

## PSF photometry

After astrometric calibration, sources in the image need to be extracted to perform photometric calibration (to compare star brightnesses to reference measurements, one first needs stars...). To do so, point spread function (PSF) photometry is employed. Each telescope has a finite aperture, therefore suffering from diffraction. Additionally, earth's atmosphere is constantly and turbulently changing, with different atmospheric layers having different refractive indices, depending on their temperature. This smears out the light from the original point source, an effect known as *seeing* (see Fig. 2.11).

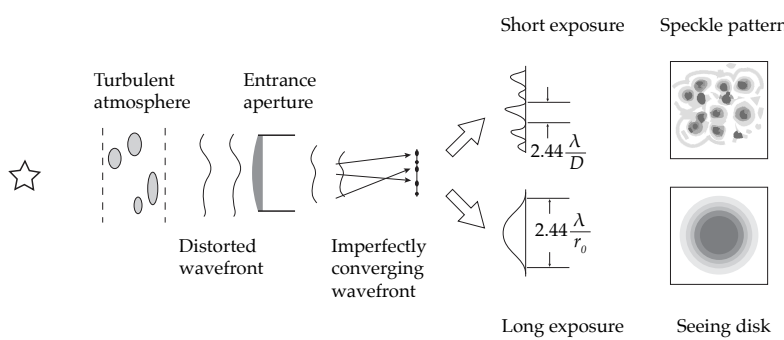


**Figure 2.11:** Seeing: Atmospheric distortions cause time-dependent distortions in the wavefronts, which average out during the exposure and form a Gaussian seeing disk on the sensor (bottom right image). Adopted from [48].

The PSF is describing the way an ideal point source is smeared out spatially after being subjected to atmospheric and optical effects in the telescope, and seeing is the FWHM of the PSF. The algorithm used to

[49]: Stetson (1987), *DAOPHOT - A computer program for crowded-field stellar photometry*

reconstruct the PSF of a ZTF exposure is DAOPhot [49]. It fits an analytic Gaussian profile to all point sources within an image. After subtracting this profile, it is iteratively updated with the residuals after subtraction. The background estimate needed for this procedure is extracted from the peak brightness value of a histogram of evenly distributed pixels within the image [49].

Of course, PS1 needs to be calibrated in itself. That is done in two steps: A self-consistent relative calibration is created with *Uberscal* [50]. This relative calibration is in turn anchored to precisely measured *Calspec* standard stars. For details, see [51]

4: This can be traced back over 2000 years to Greek/Roman astronomers Hipparchus and Ptolemy [52]. These classified the brightest stars to be of “first order” or “first magnitude”, with subsequently dimmer stars assigned lower magnitudes until the dimmest stars visible to the naked eye were of “sixth magnitude”. The system stuck and was put on firm footing by Norman Pogson in 1856. He defined a star being 5 magnitudes brighter than another one to be 100 times brighter [53].

[54]: Oke et al. (1983), *Secondary standard stars for absolute spectrophotometry*

5: The value of  $f_{\nu,0}$  is not entirely random: The traditional zero point was the star Vega. Vega’s magnitude in the AB system as defined above, integrated over the V-band, is 0.03, close to the traditional 0. The AB system has the advantage of not relying on a physical source.

[55]: Tonry et al. (2012), *The Pan-STARRS1 Photometric System*

## Photometric calibration and magnitudes

Not only the source positions in the images need to be calibrated (astrometry), but their brightness as well (photometry). To simplify matters, ZTF is photometrically calibrated against a reference survey, namely PS1. To do this, a catalog of useful calibrator stars from the PS1 survey has been curated. These stars are required to fulfill some basic quality criteria: They should be stable over multiple PS1 survey epochs in all PS1 filters excluding the  $y$ -band ( $g, r, i, z$ ) and should be fairly bright, but not so bright that they saturate the ZTF sensors. Furthermore, they are required to be fairly isolated to avoid blending with neighboring objects and need to have a high probability of being in fact stars (as opposed to galaxies) [43].

The brightness of both ZTF and PS1 are measured in magnitudes. Magnitudes are somewhat counterintuitive, as a higher value corresponds to a fainter source.<sup>4</sup> The following definition holds:

**Definition 2.4.1** A star one magnitude brighter than another star is  $\sqrt[5]{100} \approx 2.512$  times brighter

If one uses flux density (power per unit area) on earth as a measure of brightness, it follows from Def. 2.4.1 that the difference between two objects with magnitudes  $m_1$  and  $m_2$  and respective flux densities  $f_1$  and  $f_2$  is:

$$m_1 - m_2 = -2.5 \log_{10} \frac{f_1}{f_2} \quad (2.1)$$

Now we have a *relative* definition of a source’s magnitude, but we need an *absolute* one. In other words, one needs to know what constitutes a magnitude of 0 (the zero point of the magnitude scale). ZTF uses AB magnitudes [54], which are defined via the spectral flux density  $f_{\nu}$  [ $\text{W m}^{-1} \text{Hz}^{-1}$ ]. In this system, the magnitude is a logarithm of the spectral flux density:

**Definition 2.4.2**  $m_{AB}(\nu) = -2.5 \log_{10} (f_{\nu}/3631 \text{Jy})$

As one can see, a source with constant spectral flux density  $f_{\nu,0} = 3631 \times 10^{-23} \text{ W cm}^{-1} \text{Hz}^{-1} = 3631 \text{ Jy}$  corresponds to a magnitude of 0.<sup>5</sup> Now, telescopes like ZTF and PS1 use bandpass filters, so the spectral flux density is integrated over the filter wavelengths. Therefore, the magnitude definition changes to [55]:

**Definition 2.4.3**  $m = -2.5 \log_{10} \frac{\int f_{\nu}(h\nu)^{-1} A(\nu) d\nu}{\int 3631 \text{Jy} (h\nu)^{-1} A(\nu) d\nu}$

Here,  $h$  is Planck's constant and  $A(\nu)$  is the capture cross section (i.e. the chance of an incoming photon to produce an electron in the detector<sup>6</sup>). ZTF does not use a precisely modeled response function  $A(\nu)$ , but relies on PS1. To first order, ZTF magnitudes are tied to the PS1 system via their zero point:

$$m_{\text{cal}} = m_{\text{instr}} + \text{ZP} \quad (2.2)$$

To do this, all extracted sources are spatially matched to the PS1 calibrator catalog. After creating a one-to-one relation between ZTF stars and PS1 calibrator stars, one could to first order calculate  $m_{\text{cal}}$ .

But there is a potential complication: The ZTF and PS1 filters are fairly similar, but not exactly so. This means that a celestial object that does not have a constant spectrum (i.e. almost all of them) will have slightly different brightness values when measured with the ZTF and the corresponding PS1 filter. To account for this, a linear, filter-dependent *color correction*  $c_f$  needs to be applied:

$$m_{\text{cal}} = m_{\text{instr}} + \text{ZP}_f + c_f \times \text{PS1}_{\text{clr}} \quad (2.3)$$

where  $\text{PS1}_{\text{clr}}$  is filter dependent ( $g_{\text{PS1}} - r_{\text{PS1}}$  for the ZTF  $g/r$ -band, and  $r_{\text{PS1}} - i_{\text{PS1}}$  for the  $i$ -band).

In the photometric calibration step,  $\text{ZP}_f$  and  $c_f$  are chosen to globally minimize  $\Delta m_f = \text{ZP}_f + c_f \times \text{PS1}_{\text{clr}}$  for all calibrator stars in the respective image [43].

## Image subtraction

Because ZTF is a survey telescope deeply rooted in time-domain astronomy, many of the science goals concern observing sources that are *new* or *changing*. To do so, one needs to detect changes in the nightly observations with regard to *reference images*. From all new images those reference images are subtracted (see Fig. 2.12). All remaining detections constitute temporal evolution with respect to the epoch of reference image creation. All reference images in ZTF are stacked images of 15–40 individual high-quality images, mostly created while ZTF telescope operations were ramping up. Quality criteria for the individual images comprise good seeing, low errors on the astrometric and photometric calibrations, as well as background levels falling into filter-specific ranges [42].

**SWarp** [56] is used to interpolate and resample the reference image onto the science image, while subsequent subtraction and PSF photometry (see PSF photometry) is performed with the ZOGY algorithm [57].

<sup>6</sup>: More general,  $A(\nu)$  is  $A(\nu, \theta, t)$ , also depending on the angle of the incoming photon and therefore the atmospheric column along the line of sight, as well as time.

source

[56]: Bertin (2010), *SWarp: Resampling and Co-adding FITS Images Together*

[57]: Zackay et al. (2016), *Proper Image Subtraction–Optimal Transient Detection, Photometry, and Hypothesis Testing*

## Alert packages

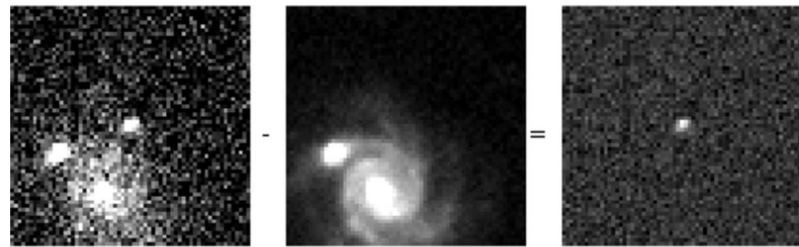


**Figure 2.12:** ZTF image subtraction. The new science image is on the left; in the middle is reference image, which is subtracted. This results in a *difference image*, seen on the right. From [58].

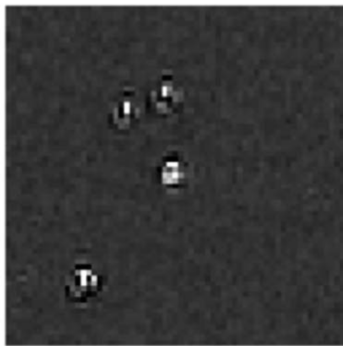


**Figure 2.13:** ZTF subtraction artifact, resulting in a bogus transient. From [58].

[58]: Mahabal et al. (2019), *Machine Learning for the Zwicky Transient Facility*

[59]: Tachibana et al. (2018), *A Morphological Classification Model to Identify Unresolved PanSTARRS1 Sources: Application in the ZTF Real-time Pipeline*

7: <https://avro.apache.org>

8: <https://kafka.apache.org>

[60]: Patterson et al. (2018), *The Zwicky Transient Facility Alert Distribution System*

[61]: Bellm et al. (2019), *The Zwicky Transient Facility: Surveys and Scheduler*

The last step in the imaging pipeline is alerting an array of upstream transient alert brokers. The information on new transients or updates on existing ones therefore need to be packaged into a convenient format. All positive detections after image subtraction with a signal-to-noise greater than 5 are subjected to a machine-learning (ML) algorithm designated to discriminate between “real” (most likely astrophysical) and “bogus” (e.g. subtraction artifacts, see Fig. 2.13) events [58]. This algorithm creates a `rbscore`, ranking the probability of the detection of being real.

Another ML algorithm has been employed to assign all PS1 sources a `sgscore`, separating between stars and galaxies based on their morphology and flux in all PS1 bands [59]. Both `rbscore` and `sgscore`, as well as cutouts of the science, reference and difference images are packed together and shipped as *alert package*. These alerts also include the distances to the three nearest PS1 sources, the closes *Gaia* source, up to 30 days of previous detections if these exist, and some quality metrics like the limiting magnitude. The file format for distribution is Apache Avro<sup>7</sup>, and the method of distribution is an Apache Kafka<sup>8</sup> stream [60].

## 2.5 Surveys and Cadence

ZTF is supporting three main survey programs: Firstly, there is the NSF Mid-Scale Innovations Program (MSIP) survey, which is allocated 40% of telescope time. The MSIP survey is subdivided into the Northern Sky Survey, using a large fraction (85%) of MSIP time. This survey covers the entire  $23\,675 \text{ deg}^2$  of the northern sky  $7^\circ$  above the galactic plane. As long as a field (see ZTF grid) is accessible, it is observed once in the *g*- and once in the *r*-band every 3 nights, with both images separated by at least 30 minutes to reject transients and moving (i.e. solar system) objects. The rest of the northern sky ( $|b| \leq 7^\circ$ , with a footprint of  $2800 \text{ deg}^2$ ) is visited twice per night, with the same observational parameters as the Northern Sky Survey [61].

## **APPENDIX**



# Bibliography

- [1] AMANDA Collaboration, E. Andrés et al. "The AMANDA neutrino telescope". In: *Nuclear Physics B - Proceedings Supplements* 77.1-3 (1999), pp. 474–485. doi: [10.1016/s0920-5632\(99\)00469-7](https://doi.org/10.1016/s0920-5632(99)00469-7) (cited on page 1).
- [2] AMANDA Collaboration, E. Andrés et al. "The AMANDA neutrino telescope: principle of operation and first results". In: *Astroparticle Physics* 13.1 (2000), pp. 1–20. doi: [10.1016/s0927-6505\(99\)00092-4](https://doi.org/10.1016/s0927-6505(99)00092-4) (cited on page 1).
- [3] M. F. L'Annunziata. *Handbook of Radioactivity Analysis. Volume 1: Radiation Physics and Detectors. Radiation Physics and Detectors*. 4th ed. Elsevier Science & Technology Books, 2020 (cited on page 1).
- [4] P. A. Cherenkov. "Visible emission of clean liquids by action of gamma radiation". In: *Doklady Akademii Nauk SSSR* 8 (1934), pp. 451–454 (cited on page 1).
- [5] L. Filöp and T. Biró. "Cherenkov radiation spectrum". In: *International Journal of Theoretical Physics* 31.1 (1992), pp. 61–74. doi: [10.1007/bf00674341](https://doi.org/10.1007/bf00674341) (cited on page 2).
- [6] H. Iams and B. Salzberg. "The Secondary Emission Phototube". In: *Proceedings of the IRE* 23.1 (1935), pp. 55–64. doi: [10.1109/jrproc.1935.227243](https://doi.org/10.1109/jrproc.1935.227243) (cited on page 2).
- [7] T. Bednarski et al. "Calibration of photomultipliers gain used in the J-PET detector". In: *Bio-Algorithms and Med-Systems* 10.1 (2014), pp. 13–17. doi: [10.1515/bams-2013-0110](https://doi.org/10.1515/bams-2013-0110) (cited on page 2).
- [8] A. Einstein. "Über einen die Erzeugung und Verwandlung des Lichtes betreffenden heuristischen Gesichtspunkt". In: *Annalen der Physik* 322.6 (1905), pp. 132–148. doi: [10.1002/andp.19053220607](https://doi.org/10.1002/andp.19053220607) (cited on page 2).
- [9] A. G. Wright. *The Photomultiplier Handbook*. Oxford University Press, 2017, p. 624 (cited on page 3).
- [10] IceCube Collaboration, R. Abbasi et al. "Calibration and characterization of the IceCube photomultiplier tube". In: *Nuclear Instruments and Methods in Physics Research Section A: Accelerators, Spectrometers, Detectors and Associated Equipment* 618.1-3 (2010), pp. 139–152. doi: [10.1016/j.nima.2010.03.102](https://doi.org/10.1016/j.nima.2010.03.102) (cited on page 3).
- [11] Icecube Collaboration, M. Aartsen et al. "The IceCube Neutrino Observatory: instrumentation and online systems". In: *Journal of Instrumentation* 12.03 (2017), P03012–P03012. doi: [10.1088/1748-0221/12/03/p03012](https://doi.org/10.1088/1748-0221/12/03/p03012) (cited on pages 3–5).
- [12] R. Abbasi et al. "IceTop: The surface component of IceCube". In: *Nuclear Instruments and Methods in Physics Research Section A: Accelerators, Spectrometers, Detectors and Associated Equipment* 700 (2013), pp. 188–220. doi: [10.1016/j.nima.2012.10.067](https://doi.org/10.1016/j.nima.2012.10.067) (cited on pages 3, 5).
- [13] M. Ahlers, K. Helbing, and C. P. de los Heros. "Probing particle physics with IceCube". In: *The European Physical Journal C* 78.11 (2018). doi: [10.1140/epjc/s10052-018-6369-9](https://doi.org/10.1140/epjc/s10052-018-6369-9) (cited on pages 4, 9).
- [14] T. Benson et al. "IceCube Enhanced Hot Water Drill functional description". In: *Annals of Glaciology* 55.68 (2014), pp. 105–114. doi: [10.3189/2014aog68a032](https://doi.org/10.3189/2014aog68a032) (cited on pages 4, 5).
- [15] IceCube Collaboration, R. Abbasi et al. "The IceCube data acquisition system: Signal capture, digitization, and timestamping". In: *Nuclear Instruments and Methods in Physics Research Section A: Accelerators, Spectrometers, Detectors and Associated Equipment* 601.3 (2009), pp. 294–316. doi: [10.1016/j.nima.2009.01.001](https://doi.org/10.1016/j.nima.2009.01.001) (cited on page 6).
- [16] IceCube Collaboration, and R. Abbasi et al. "Evidence for neutrino emission from the nearby active galaxy NGC 1068". In: *Science* 378.6619 (2022), pp. 538–543. doi: [10.1126/science.abg3395](https://doi.org/10.1126/science.abg3395) (cited on page 6).
- [17] IceCube Collaboration, M. Aartsen et al. "The IceCube realtime alert system". In: *Astroparticle Physics* 92 (2017), pp. 30–41. doi: [10.1016/j.astropartphys.2017.05.002](https://doi.org/10.1016/j.astropartphys.2017.05.002) (cited on pages 6, 8).

- [18] AMANDA Collaboration, J. Ahrens et al. "Muon track reconstruction and data selection techniques in AMANDA". In: *Nuclear Instruments and Methods in Physics Research Section A: Accelerators, Spectrometers, Detectors and Associated Equipment* 524.1-3 (2004), pp. 169–194. doi: [10.1016/j.nima.2004.01.065](https://doi.org/10.1016/j.nima.2004.01.065) (cited on pages 6–8).
- [19] C. F. Tung et al. "The Next Generation of IceCube Real-time Neutrino Alerts". In: *Proceedings of 36th International Cosmic Ray Conference — PoS(ICRC2019)*. Sissa Medialab, 2019. doi: [10.22323/1.358.1021](https://doi.org/10.22323/1.358.1021) (cited on pages 8, 10).
- [20] D. Chirkin and W. Rhode. "Propagating leptons through matter with Muon Monte Carlo (MMC)". In: (July 2004). doi: [10.48550/ARXIV.HEP-PH/0407075](https://doi.org/10.48550/ARXIV.HEP-PH/0407075) (cited on page 9).
- [21] IceCube Collaboration, M. G. Aartsen et al. "Measurement of the multi-TeV neutrino interaction cross-section with IceCube using Earth absorption". In: *Nature* 551.7682 (2017), pp. 596–600. doi: [10.1038/nature24459](https://doi.org/10.1038/nature24459) (cited on page 9).
- [22] IceCube Collaboration, M. Aartsen et al. "Evidence for High-Energy Extraterrestrial Neutrinos at the IceCube Detector". In: *Science* 342.6161 (2013). doi: [10.1126/science.1242856](https://doi.org/10.1126/science.1242856) (cited on page 10).
- [23] F. Zwicky. "Die Rotverschiebung von extragalaktischen Nebeln". In: *Helvetica Physica Acta* 6 (Jan. 1933), pp. 110–127 (cited on page 11).
- [24] W. Baade and F. Zwicky. "On Super-Novae". In: *Proceedings of the National Academy of Sciences* 20.5 (1934), pp. 254–259. doi: [10.1073/pnas.20.5.254](https://doi.org/10.1073/pnas.20.5.254) (cited on page 11).
- [25] R. G. Harrington. "The 48-inch Schmidt-type Telescope at Palomar Observatory". In: *Publications of the Astronomical Society of the Pacific* 64 (1952), p. 275. doi: [10.1086/126494](https://doi.org/10.1086/126494) (cited on page 11).
- [26] S. H. Pravdo et al. "The Near-Earth Asteroid Tracking (NEAT) Program: An Automated System for Telescope Control, Wide-Field Imaging, and Object Detection". In: *The Astronomical Journal* 117.3 (1999), pp. 1616–1633. doi: [10.1086/300769](https://doi.org/10.1086/300769) (cited on page 11).
- [27] N. M. Law et al. "The Palomar Transient Factory: System Overview, Performance, and First Results". In: *Publications of the Astronomical Society of the Pacific* 121.886 (2009), pp. 1395–1408. doi: [10.1086/648598](https://doi.org/10.1086/648598) (cited on page 11).
- [28] E. C. Bellm. "Volumetric Survey Speed: A Figure of Merit for Transient Surveys". In: *Publications of the Astronomical Society of the Pacific* 128.966 (2016), p. 084501. doi: [10.1088/1538-3873/128/966/084501](https://doi.org/10.1088/1538-3873/128/966/084501) (cited on page 11).
- [29] N. Blagorodnova et al. "The SED Machine: A Robotic Spectrograph for Fast Transient Classification". In: *Publications of the Astronomical Society of the Pacific* 130.985 (2018), p. 035003. doi: [10.1088/1538-3873/aaa53f](https://doi.org/10.1088/1538-3873/aaa53f) (cited on page 11).
- [30] B. Schmidt. "Ein lichtstarkes komafreies Spiegelsystem". In: *Mitteilungen der Hamburger Sternwarte in Bergedorf* (1938) (cited on page 12).
- [31] R. D. Cannon. "Schmidt Telescopes: Their Past, Present and Future". In: *IAU Colloq. 148: The Future Utilisation of Schmidt Telescopes*. Ed. by J. Chapman et al. Vol. 84. Astronomical Society of the Pacific Conference Series. Jan. 1995, p. 8 (cited on page 12).
- [32] *The HIPPARCOS and TYCHO catalogues. Astrometric and photometric star catalogues derived from the ESA HIPPARCOS Space Astrometry Mission*. Vol. 1200. ESA Special Publication. Jan. 1997 (cited on page 13).
- [33] D. G. Koch et al. "Kepler Mission Design, Realized Photometric Performance, and Early Science". In: *The Astrophysical Journal* 713.2 (2010), pp. L79–L86. doi: [10.1088/2041-8205/713/2/l79](https://doi.org/10.1088/2041-8205/713/2/l79) (cited on page 13).
- [34] R. Laher et al. "Processing Images from the Zwicky Transient Facility". In: *Robotic Telescopes, Student Research and Education Proceedings*, Vol 1, No 1. Our Solar Siblings, 2018. doi: [10.32374/rtsre.2017.031](https://doi.org/10.32374/rtsre.2017.031) (cited on pages 13, 16).
- [35] R. Dekany et al. "The Zwicky Transient Facility Camera". In: *SPIE Proceedings*. Ed. by C. J. Evans, L. Simard, and H. Takami. SPIE, 2016. doi: [10.1117/12.2234558](https://doi.org/10.1117/12.2234558) (cited on pages 13, 14).

- [36] E. C. Bellm et al. "The Zwicky Transient Facility: System Overview, Performance, and First Results". In: *Publications of the Astronomical Society of the Pacific* 131.995 (2019), p. 018002. doi: [10.1088/1538-3873/aaecbe](https://doi.org/10.1088/1538-3873/aaecbe) (cited on pages 13–15).
- [37] J. R. Janesick et al. "Scientific Charge-Coupled Devices". In: *Optical Engineering* 26.8 (1987). doi: [10.1117/12.7974139](https://doi.org/10.1117/12.7974139) (cited on pages 13, 14).
- [38] R. Dekany et al. "The Zwicky Transient Facility: Observing System". In: *Publications of the Astronomical Society of the Pacific* 132.1009 (2020), p. 038001. doi: [10.1088/1538-3873/ab4ca2](https://doi.org/10.1088/1538-3873/ab4ca2) (cited on pages 14–17).
- [39] D. G. York et al. "The Sloan Digital Sky Survey: Technical Summary". In: *The Astronomical Journal* 120.3 (2000), pp. 1579–1587. doi: [10.1086/301513](https://doi.org/10.1086/301513) (cited on page 15).
- [40] N. Kaiser et al. "Pan-STARRS: A Large Synoptic Survey Telescope Array". In: *SPIE Proceedings*. Ed. by J. A. Tyson and S. Wolff. SPIE, 2002. doi: [10.1117/12.457365](https://doi.org/10.1117/12.457365) (cited on page 15).
- [41] GAIA collaboration, T. Prusti et al. "The GAIA mission". In: *Astronomy and Astrophysics* 595 (2016), A1. doi: [10.1051/0004-6361/201629272](https://doi.org/10.1051/0004-6361/201629272) (cited on page 15).
- [42] F. J. Masci et al. "The Zwicky Transient Facility: Data Processing, Products, and Archive". In: *Publications of the Astronomical Society of the Pacific* 131.995 (2019), p. 018003. doi: [10.1088/1538-3873/aae8ac](https://doi.org/10.1088/1538-3873/aae8ac) (cited on pages 15, 17, 19).
- [43] F. J. Masci et al. *The ZTF Science Data System (ZDSD) – Explanatory Supplement*. 2019 (cited on pages 16–19).
- [44] S. B. Howell. *Handbook of CCD Astronomy*. Cambridge University Press, 2006 (cited on page 16).
- [45] Gaia Collaboration, A. G. A. Brown et al. "Gaia Data Release 1. Summary of the astrometric, photometric, and survey properties". In: *Astronomy and Astrophysics* 595 (2016), A2. doi: [10.1051/0004-6361/201629512](https://doi.org/10.1051/0004-6361/201629512) (cited on page 17).
- [46] E. Bertin. "Automatic Astrometric and Photometric Calibration with SCAMP". In: *Astronomical Data Analysis Software and Systems XV*. Vol. 351. Astronomical Society of the Pacific Conference Series, 2006, p. 112 (cited on page 17).
- [47] E. Bertin and S. Arnouts. "SExtractor: Software for source extraction". In: *Astronomy and Astrophysics Supplement Series* 117.2 (1996), pp. 393–404. doi: [10.1051/aas:1996164](https://doi.org/10.1051/aas:1996164) (cited on page 17).
- [48] F. R. Chromeley. *To Measure the Sky*. Cambridge University Press, 2016 (cited on page 17).
- [49] P. B. Stetson. "DAOPHOT - A computer program for crowded-field stellar photometry". In: *Publications of the Astronomical Society of the Pacific* 99 (1987), p. 191. doi: [10.1086/131977](https://doi.org/10.1086/131977) (cited on page 18).
- [50] E. F. Schlaflay et al. "Photometric Calibration of the First 1.5 Years of the Pan-STARRS1 Survey". In: *The Astrophysical Journal* 756.2 (2012), p. 158. doi: [10.1088/0004-637x/756/2/158](https://doi.org/10.1088/0004-637x/756/2/158) (cited on page 18).
- [51] E. A. Magnier et al. "Pan-STARRS Photometric and Astrometric Calibration". In: *The Astrophysical Journal Supplement Series* 251.1 (2020), p. 6. doi: [10.3847/1538-4365/abb82a](https://doi.org/10.3847/1538-4365/abb82a) (cited on page 18).
- [52] K. Krisciunas. *A Brief History of Astronomical Brightness Determination Methods at Optical Wavelengths*. 2001. doi: [10.48550/ARXIV.ASTRO-PH/0106313](https://arxiv.org/abs/astro-ph/0106313) (cited on page 18).
- [53] D. Jones. "Norman Pogson and the Definition of Stellar Magnitude". In: *Leaflet of the Astronomical Society of the Pacific* 10.469 (July 1968), pp. 145–152 (cited on page 18).
- [54] J. B. Oke and J. E. Gunn. "Secondary standard stars for absolute spectrophotometry". In: *The Astrophysical Journal* 266 (1983), p. 713. doi: [10.1086/160817](https://doi.org/10.1086/160817) (cited on page 18).
- [55] J. L. Tonry et al. "The Pan-STARRS1 Photometric System". In: *The Astrophysical Journal* 750.2 (2012), p. 99. doi: [10.1088/0004-637x/750/2/99](https://doi.org/10.1088/0004-637x/750/2/99) (cited on page 18).
- [56] E. Bertin. *SWarp: Resampling and Co-adding FITS Images Together*. Astrophysics Source Code Library, record ascl:1010.068. Oct. 2010 (cited on page 19).
- [57] B. Zackay, E. O. Ofek, and A. Gal-Yam. "Proper Image Subtraction–Optimal Transient Detection, Photometry, and Hypothesis Testing". In: *The Astrophysical Journal* 830.1 (2016), p. 27. doi: [10.3847/0004-637x/830/1/27](https://doi.org/10.3847/0004-637x/830/1/27) (cited on page 19).

- [58] A. Mahabal et al. "Machine Learning for the Zwicky Transient Facility". In: *Publications of the Astronomical Society of the Pacific* 131.997 (2019), p. 038002. doi: [10.1088/1538-3873/aaf3fa](https://doi.org/10.1088/1538-3873/aaf3fa) (cited on page 20).
- [59] Y. Tachibana and A. A. Miller. "A Morphological Classification Model to Identify Unresolved PanSTARRS1 Sources: Application in the ZTF Real-time Pipeline". In: *Publications of the Astronomical Society of the Pacific* 130.994 (2018), p. 128001. doi: [10.1088/1538-3873/aae3d9](https://doi.org/10.1088/1538-3873/aae3d9) (cited on page 20).
- [60] M. T. Patterson et al. "The Zwicky Transient Facility Alert Distribution System". In: *Publications of the Astronomical Society of the Pacific* 131.995 (2018), p. 018001. doi: [10.1088/1538-3873/aae904](https://doi.org/10.1088/1538-3873/aae904) (cited on page 20).
- [61] E. C. Bellm et al. "The Zwicky Transient Facility: Surveys and Scheduler". In: *Publications of the Astronomical Society of the Pacific* 131.1000 (2019), p. 068003. doi: [10.1088/1538-3873/ab0c2a](https://doi.org/10.1088/1538-3873/ab0c2a) (cited on page 20).